Improved Image Reconstruction for Subspace-Based Spectroscopic Imaging Using Non-Quadratic Regularization

Zheng-Hua Wu[1] *Student Member, IEEE*, Fan Lam[2] *Student Member, IEEE*, Chao Ma[3] *Member, IEEE*, Zhi-Pei Liang[2] *Fellow, IEEE*

***Abstract*— A new MR spectroscopic imaging method, called SPICE (SPectroscopic Imaging by exploiting spatiospectral CorrElation), has been recently proposed to enable high-resolution metabolic imaging with good SNR. A key problem within the SPICE framework is image reconstruction from a very noisy and sparsely sampled dataset. This paper addresses this problem by integrating the low-rank model used in SPICE reconstruction with a non-quadratic regularization. An efficient primal-dual based algorithm is described to solve the associated optimization problem. The proposed method has been validated using both simulation and phantom studies and is expected to enhance the unprecedented capability of SPICE for high-resolution metabolic imaging.**

I. INTRODUCTION

Magnetic resonance spectroscopic imaging (MRSI) can noninvasively obtain in vivo biochemical information and has been recognized as a powerful tool for many clinical and research applications [1], [2]. However, the practical utility of MRSI has been limited by long data acquisition time, intrinsically low signal-to-noise ratio (SNR) and poor spatial resolution.

Significant efforts have been made to address these challenges, resulting in a large number of novel fast sequences and advanced reconstruction schemes [2], [3], [4], [5], [6], [7]. Recently, a new MRSI method, coined SPICE (SPectroscopic Imaging by exploiting spatiospectral CorrElation), has been proposed to enable rapid high-resolution MRSI with good SNR [8]. SPICE is characterized by the use of a subspace model for both data acquisition and image reconstruction. Specifically, SPICE uses the partial separability (PS) model to represent the spatiospectral function of interest in MRSI [9], [10]. With this model, SPICE uses a hybrid CSI-EPSI pulse sequence to sample (k,t)-space in two datasets, one for estimating the subspace where the high-dimensional spectroscopic signal resides in, and the other for obtaining the final high-resolution reconstruction with the knowledge of the subspace.

Assuming the subspace can be accurately estimated from the first dataset, a remaining important problem in SPICE is the reconstruction of the spatiospectral function from the second dataset, which has extremely low SNR and is sparsely sampled in (k,t)-space. In the original SPICE framework, a low-rank representation (derived from the PS model) with a weighted-ℓ_2 regularization has been used to solve the reconstruction problem. Although the weighted-ℓ_2 regularization is advantageous in terms of computational efficiency and easier characterization, it has not fully made use of the prior information about the underlying spatiospectral distribution. Additionally, the edge information obtained from high-resolution anatomical images for the weighted-ℓ_2 regularization may not necessarily match the edge distributions of the underlying spatiospectral images, which can lead to artifacts in the reconstructions.

In this work, we explore the use of non-quadratic regularization (also widely referred to as sparsity promoting penalties) for improved SPICE reconstruction. Specifically, we propose a formulation that integrates the low-rank model in SPICE with a total variation based regularization functional. An efficient primal-dual based algorithm is described to solve the resulting large-scale optimization problem. Results from carefully designed simulation and phantom studies are used to demonstrate the improvements obtained by the proposed method over the original weighted-ℓ_2 regularization scheme.

The rest of the paper is organized as follows: Section II describes the problem formulation and the proposed primal-dual based algorithm in detail; Section III describes the experimental setup and presents some representative experiment results obtained using the proposed method, followed by conclusion in Section IV.

II. PROPOSED METHOD

A. Spatiospectral model

The (k,t)-space data $s(\mathbf{k},t)$ measured in MRSI experiments can be expressed as

$$s(\mathbf{k},t)=\iint \rho(\mathbf{r},f)e^{-i2\pi(ft+\Delta f_0(\mathbf{r})t+\mathbf{k}\cdot\mathbf{r})}df d\mathbf{r}+\xi, \quad (1)$$

where $\rho(\mathbf{r},f)$ is the spatiospectral function of interest, ξ the measurement noise (often modeled as a complex white Gaussian noise), and $\Delta f_0(\mathbf{r})$ the field inhomogeneity in Hertz.

This work was supported in part by the following research grants: P41-EB015904, P41-EB001977, 1RO1-EB013695. The first author would also like to thank Chinese Scholarship Council for support.

[1]Z. H. Wu is with the Control Science and Engineering, Harbin Institute of Technology, 92 West Da-Zhi Street, Harbin 150001, China. Z. H. Wu now is a visiting scholar in Backman Institute for Advanced Science and Technology, University of Illinois at Urbana-Champaign. zhenghuahitchina@gmail.com

[2]F. Lam and Z.-P. Liang are with the Department of Electrical and Computer Engineering and Backman Institute for Advanced Science and Technology, University of Illinois at Urbana-Champaign, 1406 West Green Street, Urbana, IL, 61801.

[3]C. Ma is with Beckman Institute for Advanced Science and Technology, Univeristy of Illinois at Urbana-Champaign, 405 N. Mathews Ave., Urbana, IL, 618101.

978-1-4244-7929-0/14/$26.00 ©2014 IEEE

To obtain a high-resolution spatiospectral distribution from $s(\mathbf{k}, t)$, SPICE models $\rho(\mathbf{r}, f)$ as

$$\rho(\mathbf{r}, f) = \sum_{l=1}^{L} u_l(\mathbf{r}) v_l(f), \tag{2}$$

where $\{u_l(\mathbf{r})\}_{l=1}^{L}$ and $\{v_l(f)\}_{l=1}^{L}$ are sets of spatial and spectral basis functions, respectively, and L is the model order (or "separation rank"). More specifically, assuming $\rho(\mathbf{r}, f)$ is defined over a given grid$(\{(\mathbf{r}_n, f_m)\}_{n,m=1}^{N,M})$, it has been shown that the PS model in Eq. (2) implies that the Casorati matrix $\mathbf{C}$ formed by $\rho(\mathbf{r}_n, f_m)$ has a low-rank structure as [9], [10], [11], [12].

$$\mathbf{C} = \mathbf{U_r} \mathbf{V}_f, \tag{3}$$

where $\mathbf{U_r} \in \mathbb{C}^{N \times L}$ and $\mathbf{V}_f \in \mathbb{C}^{L \times M}$ are rank L matrices containing the spatial and spectral basis vectors, respectively.

Based this model, two complementary datasets are acquired in SPICE: one with limited k-space coverage but dense temporal sampling, which captures full spectral information (denoted as $\mathcal{D}_1$), and the other with extended k-space coverage but sparsely sampled (k, t)-space (denoted as $\mathcal{D}_2$). The reconstruction is then done in two steps: (i) estimating $\mathbf{V}_f$ from $\mathcal{D}_1$ and (ii) estimating $\mathbf{U_r}$ and $\mathcal{D}_2$.

B. Proposed formulation

Given the low-rank model in Eq. (3) and a predetermined $\mathbf{V}_f$ (denoted as $\hat{\mathbf{V}}_f$), we propose to estimate $\mathbf{U_r}$ using the following formulation:

$$\hat{\mathbf{U}}_\mathbf{r} = \underset{\mathbf{U_r}}{\operatorname{argmin}} \frac{1}{2\lambda} \|\mathbf{d} - \mathbf{\Omega F B}\{\mathbf{U_r} \hat{\mathbf{V}}_t\}\|_2^2 + R(\cdot), \tag{4}$$

where $\hat{\mathbf{V}}_t$ is the inverse Fourier transform of $\hat{\mathbf{V}}_f$, $\mathbf{d}$ is a vector containing the data in $\mathcal{D}_2$, $\mathbf{F}$ denotes the discrete Fourier transform operator, $\mathbf{B}$ is a linear operator incorporating the B_0 field inhomogeneity effects and $\mathbf{\Omega}$ is a sampling operator. $R(\cdot)$ is the regularization term and λ is a regularization parameter.

In particular, we consider non-quadratic regularization functional for $R(\mathbf{U_r} \hat{\mathbf{V}}_t \mathbf{F}_t)$, where $\mathbf{F}_t$ is a temporal Fourier transform matrix. Specifically, the widely used total variation (TV) penalty and the total generalized variation (TGV) penalty are considered in this paper [13], [14]. Both of these two penalties have been demonstrated effective in improving reconstruction quality by promoting sparsity of the unknown image. The motivation for choosing TGV is to reduce the staircasing artifacts typically present in TV regularized reconstructions by utilizing higher-order derivatives. TGV can also maintain the advantages of TV in terms of edge preservation and noise removal by offering a balance between higher-order and lower-order derivatives. Specifically, we will choose the second-order TGV in this paper based on the tradeoff between computation complexity and performance shown in the exiting literatures [13]. It is also worth noting that a similar form of TGV regularization has been previously used in [15] but for super-resolution reconstruction from low-resolution CSI data without predetermining the subspace.

C. Algorithms

In this section, we first present a primal-dual based algorithm to solve Eq. (4) with second-order TGV penalty. Then the algorithm for TV penalty will be briefly described as a special case of the general algorithmic framework.

Based on the following definition of the discrete form of the second-order TGV

$$\mathbf{TGV}_2^\alpha(\mathbf{u}) = \min_{\mathbf{w}} \alpha_1 \|\nabla \mathbf{u} - \mathbf{w}\|_1 + \alpha_0 \|\varepsilon(\mathbf{w})\|_1, \tag{5}$$

where $\nabla \mathbf{u}$ is the gradient of $\mathbf{u}$, $\varepsilon(\mathbf{w}) = \frac{1}{2}(\nabla \mathbf{w} + \nabla \mathbf{w}^H)$ represents the symmetrized gradient, α_1 and α_0 are the parameters to balance the first and second-order derivatives, we can formulate the TGV regularized reconstruction as

$$\begin{aligned}\{\hat{\mathbf{U}}_\mathbf{r}, \hat{\mathbf{w}}\} = \arg \min_{\mathbf{U_r}, \mathbf{w} \in \mathbb{C}^{2MN \times 1}} & \frac{1}{2\lambda} \|\mathbf{d} - \mathbf{\Omega F B}\{\mathbf{U_r} \hat{\mathbf{V}}_t\}\|_2^2 \\ & + \alpha_1 \|\nabla(\mathbf{U_r} \hat{\mathbf{V}}_t \mathbf{F}_t) - \mathbf{w}\|_1 + \alpha_0 \|\varepsilon(\mathbf{w})\|_1. \end{aligned} \tag{6}$$

We then reformulate Eq. (6) as the following convex-concave saddle-point problem with respect to the data fitting term

$$\begin{aligned}\{\hat{\mathbf{U}}_\mathbf{r}, \hat{\mathbf{w}}, \hat{\mathbf{p}}, \hat{\mathbf{q}}, \hat{\mathbf{e}}\} = \arg \min_{\mathbf{U_r}, \mathbf{w}} \max_{\mathbf{p} \in P, \mathbf{q} \in Q, \mathbf{e}} & \langle \nabla(\mathbf{U_r} \hat{\mathbf{V}}_t \mathbf{F}_t) - \mathbf{w}, \mathbf{p} \rangle \\ & + \langle \varepsilon(\mathbf{w}), \mathbf{q} \rangle + \langle \mathbf{\Omega F B}\{\mathbf{U_r} \hat{\mathbf{V}}_t\} - \mathbf{d}, \mathbf{e} \rangle - \frac{\lambda}{2} \|\mathbf{e}\|_2^2, \end{aligned} \tag{7}$$

where $\mathbf{e} \in \mathbb{C}^{D \times 1}$, $P = \{\mathbf{p} \in \mathbb{C}^{2NM \times 1} | \|\mathbf{p}\|_\infty \leq \alpha_1\}$ and $Q = \{\mathbf{q} \in \mathbb{C}^{3NM \times 1} | \|\mathbf{q}\|_\infty \leq \alpha_0\}$. Based on the primal-dual algorithm [14], we can solve Eq. (7) using the following iterative procedures:

- $\mathbf{p}^{(i+1)} = Proj_P(\mathbf{p}^{(i)} + \delta(\nabla(\bar{\mathbf{U}}_\mathbf{r}^{(i)} \hat{\mathbf{V}}_t \mathbf{F}_t) - \bar{\mathbf{w}}^{(i)}))$
- $\mathbf{q}^{(i+1)} = Proj_Q(\mathbf{q}^{(i)} + \delta \varepsilon(\bar{\mathbf{w}}^{(i)}))$
- $\mathbf{e}^{(i+1)} = Prox_2^\alpha(\mathbf{e}^{(i)} + \delta(\mathbf{\Omega F B}\{\bar{\mathbf{U}}_\mathbf{r}^{(i)} \hat{\mathbf{V}}_t\} - \mathbf{d}))$
- $\mathbf{U}_\mathbf{r}^{old} = \mathbf{U}_\mathbf{r}^{(i)}$
- $\mathbf{U}_\mathbf{r}^{(i+1)} = \mathbf{U}_\mathbf{r}^{(i)} + \tau((div_1 \mathbf{p}^{(i+1)}) \mathbf{F}_t^H \hat{\mathbf{V}}_t^H - ((\mathbf{B}^* \mathbf{F}^* \mathbf{\Omega}^* (\mathbf{e}^{(i+1)})) \hat{\mathbf{V}}_t^H))$
- $\bar{\mathbf{U}}_\mathbf{r}^{(i+1)} = 2\mathbf{U}_\mathbf{r}^{(i+1)} - \mathbf{U}_\mathbf{r}^{old}$
- $\mathbf{w}^{old} = \mathbf{w}^{(i)}$
- $\mathbf{w}^{(i+1)} = \mathbf{w}^{(i)} + \tau(\mathbf{p}^{(i+1)} + div_2 \mathbf{q}^{(i+1)})$
- $\bar{\mathbf{w}}^{(i+1)} = 2\mathbf{w}^{(i+1)} - \mathbf{w}^{old}$

where the Euclidean projectors $Proj_P$ and $Proj_Q$ are computed as $Proj_P(\bar{\mathbf{p}}) = \bar{\mathbf{p}}/(\max(1, |\bar{\mathbf{p}}|/\alpha_1))$ and $Proj_Q(\bar{\mathbf{q}}) = \bar{\mathbf{q}}/(\max(1, |\bar{\mathbf{q}}|/\alpha_0))$, $Prox_2^\delta(\bar{\mathbf{e}}) = \bar{\mathbf{e}}/(1+\delta\lambda)$ is the proximal map, and A^* denotes the adjoint operator of A. Note that we chose divergence operators as the adjoint operators of the above differential operators, i.e. $(div_1)^* = -\nabla$ and $(div_2)^* = -\varepsilon$. The concrete forms of ∇, ε, div_1 and div_2 can be found in [16]. We chose α_0 and α_1 as $\alpha_0 = 2\alpha_1$, and initialized the variables to be $\mathbf{0}$ in this paper. Moreover, the step-sizes were chosen as $\delta = \tau = 1/\sqrt{12}$ in the simulations and $\delta = \tau = 0.06$ in the phantom studies [17].

When $R(\cdot)$ is the TV penalty, Eq. (4) can be rewritten as

$$\hat{\mathbf{U}}_\mathbf{r} = \underset{\mathbf{U}_\mathbf{r}}{\operatorname{argmin}} \frac{1}{2\lambda} \|\mathbf{d} - \mathbf{\Omega F B}\{\mathbf{U}_\mathbf{r}\hat{\mathbf{V}}_t\}\|_2^2 + \|\nabla(\mathbf{U}_\mathbf{r}\hat{\mathbf{V}}_t\mathbf{F}_t)\|_1, \quad (8)$$

which can be viewed as a special case of Eq. (6) with $\alpha_1 = 1$ and $\mathbf{w} = \mathbf{0}$. Therefore, we just need to let $\bar{\mathbf{w}} = \mathbf{0}, \mathbf{q} = \mathbf{0}, \mathbf{w} = \mathbf{0}$ and $Proj_P(\bar{\mathbf{p}}) = \bar{\mathbf{p}}/(\max(1, |\bar{\mathbf{p}}|))$ in the above iterations, and the modified procedures can then be used to solve Eq. (8). With $\hat{\mathbf{U}}_\mathbf{r}$ estimated, the final reconstruction is obtained by $\hat{\mathbf{U}}_\mathbf{r}\hat{\mathbf{V}}_f$.

III. RESULTS AND DISCUSSION

Simulated data from a carefully designed numerical brain MRSI phantom has been used to evaluate the performance of the proposed method. The phantom contains metabolite spectra (e.g., N-acetylaspartate (NAA), creatine (Cre), choline (Cho), glutamate (Glu), glutamine (Gln) and myo-inositol (Myo)) generated from quantum mechanical simulations with additions of realistic lineshape parameters and baseline signals. Spatial variations of the spectra were incorporated based on reported literature concentration ratios in gray matter, white matter and cerebrospinal fluid. Experimentally acquired anatomical image and T_2^* map were also used to increase the complexity of the spatiospectral distribution (please refer to [10] for further details on the phantom).

(k, t)-space data with field inhomogeneity effects introduced via a co-registered experimentally obtained field map were generated using the sampling patterns described in SPICE [8] (based on Eq. (1)). Specifically, $\mathcal{D}_1$ contains 8×8 CSI encodings and $\mathcal{D}_2$ contains 48 echoshifts averaged 6 times (a total of 352 excitations). An approximately equivalent-time conventional CSI acquisition [1] with only 19×19 encodings and an EPSI acquisition [2] with 128×128 encodings averaged 3 times were also generated. Conjugate phase reconstruction was applied to the CSI and EPSI data while the proposed method was applied to the data generated by SPICE acquisition. $\hat{\mathbf{V}}_f$ was estimated using the scheme described in [8] and rank 8 was chosen for reconstruction. Moreover, SPICE reconstruction with a weighted-ℓ_2 regularization (as in [8]) was also performed for comparison. Note that we selected the regularization parameter such that different regularization schemes yield a similar data consistency measure. To better illustrate the performance, the relative ℓ_2 error defined as $e = \|\hat{\rho}(\mathbf{r}, f) - \rho(\mathbf{r}, f)\|_2 / \|\rho(\mathbf{r}, f)\|_2$ was also used to compare different reconstructions, where $\hat{\rho}(\mathbf{r}, f)$ denotes the reconstructed spatiospectral distribution from different methods.

Figures 1 and 2 show a set of representative simulation results. As can be seen, with approximately the same acquisition time, SPICE reconstruction (with different regularizers) has a significantly higher resolution than CSI reconstruction, and significantly higher SNR than EPSI reconstruction. Comparing SPICE reconstructions with different regularization terms, we can observe that although they lead to similar spectra (Fig. 2) the non-quadratic penalties provide superior

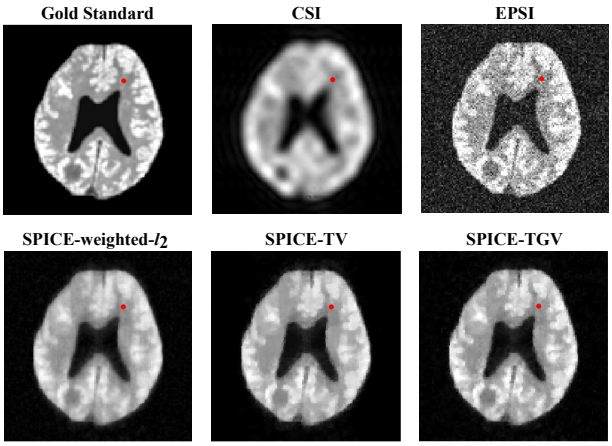

Fig. 1: Spatial maps of the frequency component at 347 Hz obtained by different reconstruction methods from the simulated data. As can be seen, the CSI reconstruction suffers from low-resolution artifacts due to limited data, and the EPSI reconstruction is very noisy due to fast acquisition, while the SPICE reconstructions have both high SNR and high-resolution.

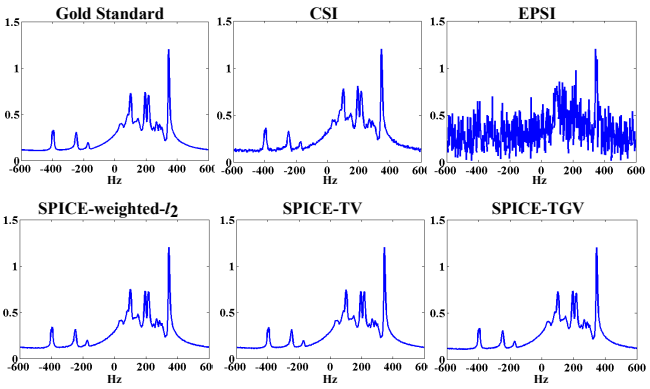

Fig. 2: Representative spectra from different reconstructions corresponding to the voxel identified by the red dot in Fig. 1.

quality in the spatial distributions (Fig. 1), i.e., better edge preservation and less oversmoothing. Particularly, the second-order TGV penalty offers the best reconstruction quality. Furthermore, the relative ℓ_2 errors from CSI, EPSI, SPICE with weighted-ℓ_2, SPICE with TV and SPICE with TGV are 0.2158, 0.3709, 0.1434, 0.1399 and 0.1244, respectively, which is consistent with the qualitative comparison.

Experimental data from a customized metabolite phantom have also been acquired to evaluate the proposed method. The phantom is a polymethylpentene cylindrical jar containing NaCl-doped water and three rows of vials with different diameters. The vials were filled with metabolite solutions (NAA, Cre, Cho and Myo) of physiologically relevant concentrations [1]. The data was acquired on a Siemens Trio 3T scanner using a customized hybrid CSI-EPSI sequence. For the SPICE acquisition, $\mathcal{D}_1$ contains 12×12 CSI encodings and $\mathcal{D}_2$ contains 100×100 EPSI encodings with one temporal interleave and 5 averages. An equivalent-time CSI acquisition with 34×34 encodings was also performed for comparison. Other relevant imaging parameters are (for both CSI and

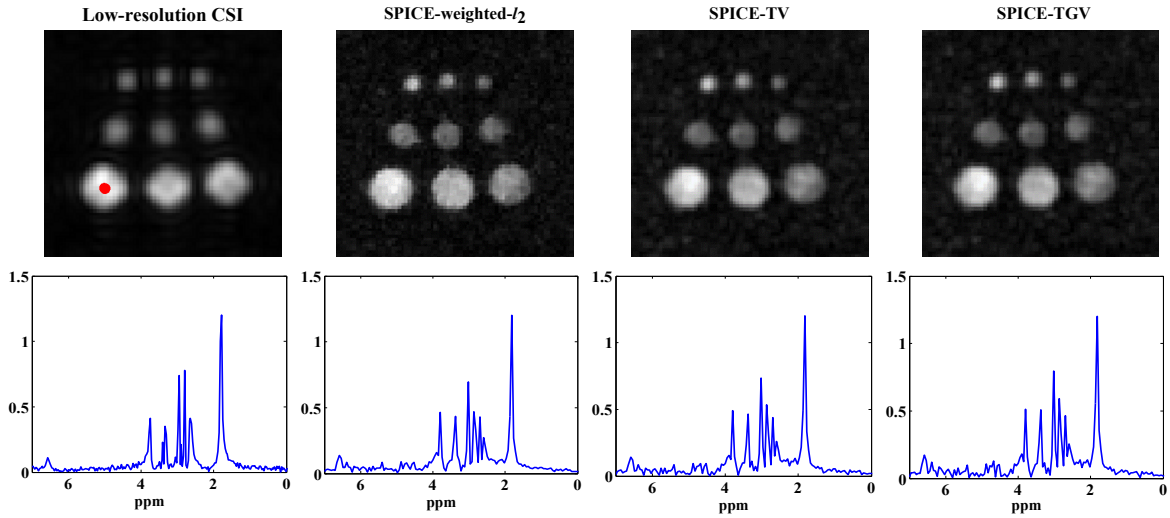

Fig. 3: Experimental results from the metabolite phantom. Top row: spatial distributions of NAA from the low-resolution CSI, SPICE with weighted-ℓ_2 regularization, SPICE with TV regularization, and SPICE with TGV regularization. Bottom row: representative spectra from different reconstructions corresponding to the voxel identified by the red dot in the first image. Note that all acquisitions took approximately the same time.

SPICE): TR/TE=1000/30 ms, FOV=220 $\times$ 220 mm^2, slice thickness=10 mm, and readout bandwidth=100 kHz.

Figure 3 presents a set of experimental results from the metabolite phantom. As expected, the low-resolution CSI reconstruction has strong truncation artifacts although it has high SNR, while SPICE reconstructions show both high spatial resolution and high SNR. Comparing SPICE reconstructions with different regularization terms, SPICE with non-quadratic penalties demonstrate better visual quality, especially in the spatial domain. But note that the second-order TGV did not seem to offer better performance than TV penalty in this case because the phantom is piecewise constant.

IV. CONCLUSION

This paper has presented a non-quadratic regularization formulation (specifically with TV and TGV) to improve image reconstruction for a recently proposed subspace-based MRSI method named SPICE. An efficient primal-dual based algorithm has been described to solve the corresponding optimization problem. Results from computer simulations and phantom studies demonstrate the improvement in the high-resolution spatiospectral reconstruction obtained by the proposed method. We expect the proposed method to be an integral part of SPICE, which can further enhance its capability for high-resolution metabolic imaging.

REFERENCES

[1] R. A. de Graaf, *In vivo NMR spectroscopy*, 2nd, ed. New York: Wiley, 2007.

[2] S. Posse, R. Otazo, S. R. Dager, and J. Alger, "MR spectroscopic imaging: principles and recent advances," *Journal of Magnetic Resonance Imaging*, vol. 37, no. 6, pp. 1301–1325, 2013.

[3] F.-H. Lin, S.-Y. Tsai, R. Otazo, A. Caprihan, L. L. Wald, J. W. Belliveau, and S. Posse, "Sensitivity-encoded (SENSE) proton echo-planar spectroscopic imaging (PEPSI) in the human brain," *Magnetic Resonance in Medicine*, vol. 57, no. 2, pp. 249–257, 2007.

[4] Z.-P. Liang and P. C. Lauterbur, "A generalized series approach to MR spectroscopic imaging," *IEEE Transactions on Medical Imaging*, vol. 10, no. 2, pp. 132–137, 1991.

[5] J. P. Haldar, D. Hernando, S.-K. Song, and Z.-P. Liang, "Anatomically constrained reconstruction from noisy data," *Magnetic Resonance in Medicine*, vol. 59, no. 4, pp. 810–818, 2008.

[6] S. Hu, M. Lustig, A. P. Chen, J. Crane, A. Kerr, D. AC. Kelley, R. Hurd, J. Kurhanewicz, S. J. Nelson, J. M. Pauly, et al., "Compressed sensing for resolution enhancement of hyperpolarized 13C flyback 3D-MRSI," *Journal of magnetic resonance*, vol. 192, no. 2, pp. 258–264, 2008.

[7] R. Eslami and M. Jacob, "Robust reconstruction of MRSI data using a sparse spectral model and high resolution MRI priors," *IEEE Transactions on Medical Imaging*, vol. 29, pp. 1297 – 1309, 2010.

[8] F. Lam and Z.-P. Liang, "A subspace approach to high–resolution spectroscopic imaging," *Magnetic Resonance in Medicine*, vol. 71, pp. 1349 – 1357, 2014.

[9] Z.-P. Liang, "Spatiotemporal imagingwith partially separable functions," in *Proc. IEEE International Symposium on Biomedical Imaging: From Nano to Macro*, 2007, pp. 988–991.

[10] H. M. Nguyen, X. Peng, M. N. Do, and Z.-P. Liang, "Denoising MR spectroscopic imaging data with low-rank approximations," *IEEE Transactions on Biomedical Engineering*, vol. 60, pp. 78–89, 2013.

[11] B. Zhao, J. P. Haldar, A. G. Christodoulou, and Z.-P. Liang, "Image reconstruction from highly undersampled (**k**, t)-space data with joint partial separability and sparsity constraints," *IEEE Transactions on Medical Imaging*, vol. 31, pp. 1809–1820, 2012.

[12] J. P. Haldar and Z.-P. Liang, "Spatiotemporal imaging with partially separable functions: a matrix recovery approach," in *Proc. IEEE International Symposium on Biomedical Imaging: From Nano to Macro*, 2010, pp. 716–719.

[13] K. Bredies, K. Kunisch, and T. Pock, "Total generalized variation," *SIAM Journal on Imaging Sciences*, vol. 3, no. 3, pp. 492–526, 2010.

[14] F. Knoll, K. Bredies, T. Pock, and R. Stollberger, "Second order total generalized variation (TGV) for MRI," *Magnetic resonance in medicine*, vol. 65, no. 2, pp. 480–491, 2011.

[15] J. Kasten, F. Lazeyras, and D. Van De Ville, "Data-driven MRSI spectral localization via low-rank component analysis," *IEEE Transactions on Medical Imaging*, 2013.

[16] B. Kristian, "Recovering piecewise smooth multichannel images by minimization of convex functionals with total generalized variation penalty," in *Inst. Math. Sci. Comput., Graz Univ. Technol., Graz, Austria, Tech. Rep, 12-006*, 2012.

[17] A. Chambolle and T. Pock, "A first-order primal-dual algorithm for convex problems with applications to imaging," *Journal of Mathematical Imaging and Vision*, vol. 40, no. 1, pp. 120–145, 2011.